Understanding shock dynamics in the inner heliosphere with modeling and Type II radio data: The 2010-04-03 event

H. Xie,[1] D. Odstrcil,[2] L. Mays,[3] O. C. St. Cyr,[4] N. Gopalswamy,[4] and H. Cremades[5]

Received 26 October 2011; revised 17 February 2012; accepted 26 February 2012; published 21 April 2012.

[1] The 2010 April 03 solar event was studied using observations from STEREO SECCHI, SOHO LASCO, and Wind kilometric Type II data (kmTII) combined with WSA-Cone-ENLIL model simulations performed at the Community Coordinated Modeling Center (CCMC). In particular, we identified the origin of the coronal mass ejection (CME) using STEREO EUVI and SOHO EIT images. A flux-rope model was fit to the SECCHI A and B, and LASCO images to determine the CME's direction, size, and actual speed. J-maps from STEREO COR2/HI-1/HI-2 and simulations from CCMC were used to study the formation and evolution of the shock in the inner heliosphere. In addition, we also studied the time-distance profile of the shock propagation from kmTII radio burst observations. The J-maps together with in-situ data from the Wind spacecraft provided an opportunity to validate the simulation results and the kmTII prediction. Here we report on a comparison of two methods of predicting interplanetary shock arrival time: the ENLIL model and the kmTII method; and investigate whether or not using the ENLIL model density improves the kmTII prediction. We found that the ENLIL model predicted the kinematics of shock evolution well. The shock arrival times (SAT) and linear-fit shock velocities in the ENLIL model agreed well with those measurements in the J-maps along both the CME leading edge and the Sun-Earth line. The ENLIL model also reproduced most of the large scale structures of the shock propagation and gave the SAT prediction at Earth with an error of $\sim$1 $\pm$ 7 hours. The kmTII method predicted the SAT at Earth with an error of $\sim$15 hours when using $n_0 = 4.16$ cm^{-3}, the ENLIL model plasma density near Earth; but it improved to $\sim$2 hours when using $n_0 = 6.64$ cm^{-3}, the model density near the CME leading edge at 1 AU.

Citation: Xie, H., D. Odstrcil, L. Mays, O. C. St. Cyr, N. Gopalswamy, and H. Cremades (2012), Understanding shock dynamics in the inner heliosphere with modeling and Type II radio data: The 2010-04-03 event, *J. Geophys. Res.*, *117*, A04105, doi:10.1029/2011JA017304.

1. Introduction

[2] For decades ground-based telescopes have detected the slowly drifting (downward in frequency) solar radio emissions at metric wavelengths called "Type II" radio bursts. When a shock travels outward from the solar corona, it accelerates electrons that in turn produce radio emission at the local plasma frequency (f_p [kHz] = 9 $\sqrt{n_e}$ [cm^{-3}]) and its first harmonic ($2f_p$). As the shock encounters less-dense regions the local plasma frequency decreases giving rise to the slow-drift. These radio emissions can start at frequencies below 150 MHz in the low corona and extend down to the kilometric domain, slowly drifting to lower frequencies all the way to 1 AU, where the local plasma frequency of the solar wind is $\sim$25 kHz [*Gopalswamy et al.*, 2005a]. Since Earth's ionosphere blocks radio signals at frequencies below $\sim$10 MHz, the only way to detect the longer-wavelength emissions is by means of instruments in interplanetary space. These emissions have been regularly detected by the Wind Radio and Plasma Wave (WAVES) experiment [*Bougeret et al.*, 1995] and more recently by the Solar Terrestrial Relations Observatory (STEREO) WAVES [*Bougeret et al.*, 2008], whose space weather beacon makes them available in near-real-time.

[3] Recently *Cremades et al.* [2007] described a novel technique to predict interplanetary (IP) shock arrival at L1 by measuring the drift rate of the kilometric ($\leq$300 kHz) Type II (kmTII) emissions. Shocks between 1997–2004 were identified from catalogues maintained by Wind and Advanced Composition Explorer (ACE) investigators, and

[1]Department of Physics, Catholic University of America, Washington, DC, USA.
[2]Department of Computational and Data Sciences, George Mason University, Fairfax, Virginia, USA.
[3]NASA Postdoctoral Program Fellow, Oak Ridge Associated Universities, Oak Ridge, Tennessee, USA.
[4]NASA Goddard Space Flight Center, Greenbelt, Maryland, USA.
[5]UTN-FRM/CONICET, Mendoza, Argentina.

0148-0227/12/2011JA017304

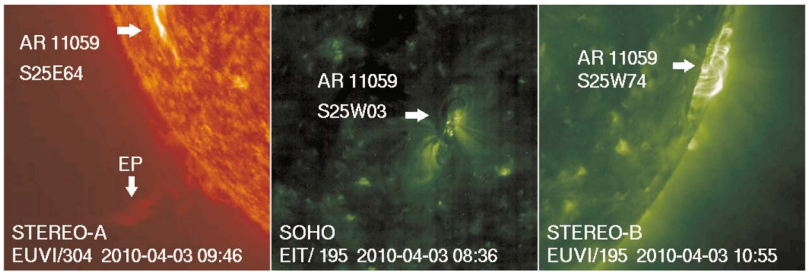

Figure 1. (left) EUVI 304 *Å* image on STEREO A showing an eruptive prominence to the south of AR 11059 at 09:46 UT; (middle) EIT 195 *Å* image at 08:36 UT and (right) EUVI 195 *Å* image at 10:55 UT showing a sigmoid to post eruption arcade flare in AR 11059 observed from SOHO and STEREO B, respectively.

altogether 160 kmTII radio bursts were identified in the Wind WAVES data set. A subset of 84 kmTII events could be reliably measured and used to make a prediction as to when the shock should be seen at L1. 66% of the predictions were within ±6 hours of the actual shock arrival time, and space weather forecasters have shown keen interest in incorporating this technique into their forecasts.

[4] STEREO is comprised of two identical spacecraft orbiting the Sun ahead STEREO-A (STA) and behind STEREO-B (STB) Earth near the ecliptic plane [*Kaiser et al.*, 2008]. The two spacecraft separate away from Earth at a rate of about 22° per year. The extended solar minimum of 2007–2009 did not provide many earthward halo CMEs for the two STEREO spacecraft to study, but on April 3, 2010 a fast CME was observed to propagate toward Earth. The April 3 CME produced an interplanetary (IP) shock followed by an IP coronal mass ejection (ICME), which caused an extended geomagnetic storm with minimum Dst = −72 nT on April 5–7, 2010. During the storm, communication with the Galaxy 15 satellite was lost (W. Ferster, Intelsat Loses Contact with Galaxy 15 Satellite, Space News, 8 April 2010). Both STA [STB] observed the CME expanding off the West [East] limb around 09:00 UT; the Large Angle and Spectrometric Coronagraph Experiment (LASCO) [*Brueckner et al.*, 1995] on board the Solar and Heliospheric Observatory (SOHO) observed the CME appearing as a halo event around 10:33 UT. The separation angles of STA [STB] with Earth were 67° [71°]. When we include SOHO, the three spacecraft (STA/B and SOHO) provided almost ∼140° view of the event. The Sun Earth Connection Coronal and Heliospheric Investigation (SECCHI) instrument package includes: the inner and outer coronagraph (COR1 and COR2), and the Heliospheric Imagers (HI1 and HI2) [*Eyles et al.*, 2009]. STEREO successfully tracked the April 3, 2010 event from the Sun into the heliosphere all the way to 1 AU. HI1 and HI2 image movies on STA showed clearly the evolution of the CME-driven shock in the heliosphere (see auxiliary material).[1] Furthermore, a kmTII radio burst was detected by Wind WAVES [*Bougeret et al.*, 1995] on April 4 from 00:58 until 16:33 UT. The associated shock arrived at the Wind spacecraft on April 5 07:48 UT. The wealth of data for this event provides us with a good opportunity to study the formation and the evolution of the CME-driven shock and to validate different methods of modeling and predicting IP shock dynamics and arrival time.

[5] The April 3, 2010 event has been studied by several authors. *Möstl et al.* [2010] carried out an analysis of the in situ data of the associated IP shock and ICME that drove the shock. They showed that the ICME was a magnetic-cloud-like structure but it could not be fitted by any magnetic cloud models. By linking STEREO/SECCHI images to in situ observations, they demonstrated that the apex of the ICME was southward directed and only its northern flank passed over Earth. *Wood et al.* [2011] performed a thorough white-light analysis of the CME using an empirical flux-rope reconstruction and demonstrated that the CME could be fitted reasonably well with a 3D flux rope shape, where its orientation angle out of the ecliptic plane has been rotated from −80° (i.e., nearly N-S) close to the Sun to 10° (i.e., nearly E-W) far from the Sun. Using combined STEREO SECCHI imaging and the modeling of the CME driven shock, *Rouillard et al.* [2011] investigated the corresponding solar energetic particle (SEP) events measured at L1 and STB, and associated the origin and magnitude of the SEP event with the shock properties along different interplanetary magnetic field (IMF) lines.

[6] In this paper, we perform a comprehensive study on the evolution and propagation of the April 3, 2010 CME/shock, combining STEREO and SOHO white light observations, kmTII radio data with the WSA-Cone-ENLIL model simulation. We use a flux rope model [e.g., *Krall and St. Cyr*, 2006; *Xie et al.*, 2009] fit to SECCHI and LASCO observations to determine the CME speed, size and direction, as well as its time-distance profile when the CME is close to the Sun. To fully investigate the IP shock dynamics we use a heliospheric WSA-Cone-ENLIL simulation model. The fitted CME radial speed and half angular width are used to specify a hydrodynamic spherical cloud launched into the heliospheric computational domain. We derive the time-distance profile of the CME-driven shock in the heliosphere from J-maps (plots of elongation from the Sun versus time along fixed position angles [e.g., *Sheeley et al.*, 1999, 2008]) constructed from SECCHI images. The simulation results are directly compared with the SECCHI observations. We focus on two aspects in the paper: (1) using SECCHI and radio data to constrain the ENLIL model output and (2) determining whether or not a combination of techniques yields an improved prediction.

[1]Auxiliary materials are available in the HTML. doi:10.1029/2011JA017304.

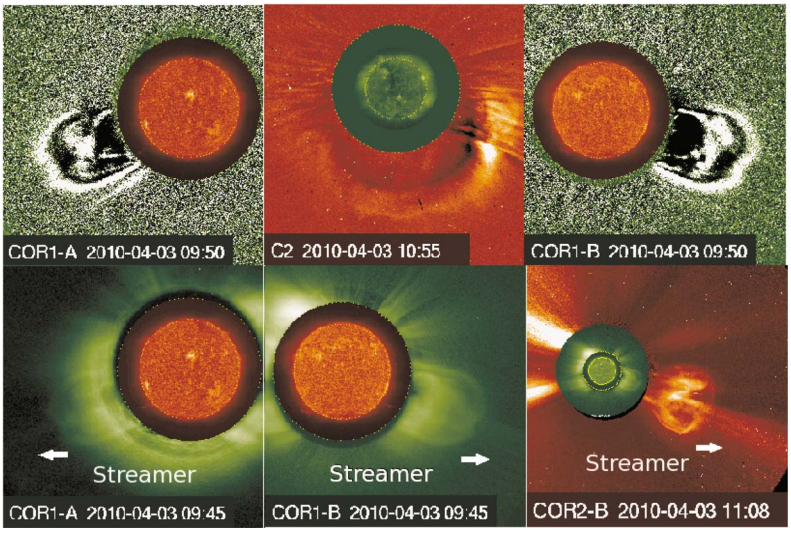

Figure 2. (top left) STEREO A and (top right) B COR1 running-difference images superimposed with EUVI 304 *Å* image at 09:50 UT and (top middle) SOHO C2 running-difference image superimposed with EIT 195 *Å* image at 10:55 UT showing edge-on and face-on views of the April 03 CME. (bottom left) STEREO A and (bottom middle) B COR1 original images superimposed with EUVI 304 *Å* image at 09:45 UT and (bottom right) STEREO B COR2 image at 11:08 UT showing a streamer located ahead of the CME leading edge.

[7] The paper is organized as follows: Section 2 presents the observations, including the CME solar source, flux rope model fit to coronagraphic images, and kinematic analysis with J-maps. Section 3 describes the WSA-Cone-ENLIL model simulation, and Section 4 gives the simulation results and comparison between the simulation results and observations. Section 5 introduces the kmTII technique and applies the ENLIL model results to the method to improve the prediction. Finally, the discussion and conclusions are presented in Section 6.

2. Observations

2.1. CME Solar Source

[8] The April 3, 2010 CME was an Earth-directed CME, which was associated with a X-ray flare with a peak flux level of B7.4 recorded by GOES X-ray monitor from NOAA Active Region (AR) 11059 (S25W03) between 09:04 UT and 10:58 UT, with a peak at 09:54 UT. The flare was first seen in the Extreme Ultraviolet Imaging Telescope (EIT) on board SOHO between 09:14 UT and 10:00 UT with a faint EIT wave associated with the flare (http://cdaw.gsfc.nasa.gov/movie/make_javamovie.php?date=20100403&img1=soh_e195). The evolution of the flare showed a clear sigmoid to post-arcade structure, and the neutral line in the sigmoid active region was tilted ~80° relative to the horizontal (east-west) direction (Figure 1, middle). On April 3, the separation angles of STA and STB with Earth are 67° and 71°, respectively. The flare was observed at S25E64 from STA and S25W74 from STB. An eruptive prominence (EP) was observed to the south of AR 11059 by SECCHI's Extreme Ultraviolet Imager (EUVI) at 304 *Å* on STA at 09:46 UT, as shown in Figure 1 (left). The prominence began to be active around 08:56 UT and erupted around 09:16 UT. EUVI 304 *Å* movie and EIT 195 *Å* movies show that both the prominence eruption and the X-ray flare eruption are related to the CME and the EP appeared as the CME core in COR1 around 10:15 UT. The flare location and post-eruption arcade are shown in Figure 1 (right) as observed by EUVI 195 *Å* on STB at 11:00 UT.

2.2. CME Speed, Width and Propagation Direction: Flux Rope Model Fit

[9] The CME was seen edge-on by COR1-A off the southeast limb starting at 09:05 UT, and by COR1-B off the

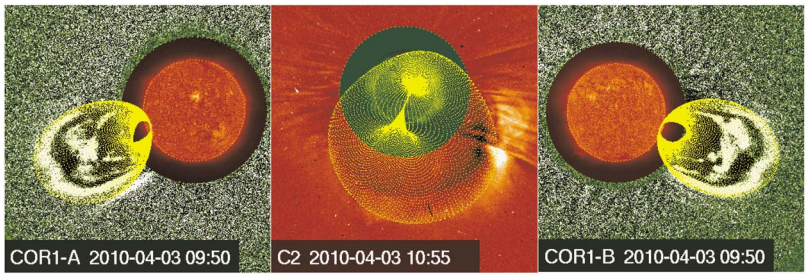

Figure 3. Flux-rope Modeling of the Apr 3, 2010 CME. STEREO A and B COR1 and SOHO C2 images with the flux-rope projected wireframe (yellow curves) overlaid on top.

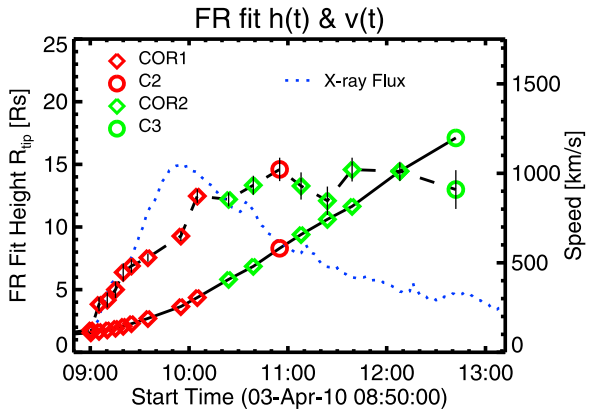

Figure 4. The flux-rope model fit results to the CME in COR1 (red diamonds), COR2 (green diamonds), C2 (red open circles), and C3 (green open circles) images. The model fit height-time profile and derived velocity profile are denoted by the solid and dashed lines, respectively, overplotted with the GOES X-ray flux (blue dotted line). The short vertical lines in the figure indicate the velocity uncertainties.

southwest limb (http://cor1.gsfc.nasa.gov/catalog/). LASCO observed a halo CME on April 3 and its first appearance time in LASCO C2 was 10:33 UT (http://cdaw.gsfc.nasa.gov/CME_list). In Figure 2, we show the CME running difference images from STA/B COR1 and SOHO C2, respectively, along with the COR1(STA/B) and COR2-B original images at bottom panel. In COR2-B original image, a streamer ahead of the CME leading edge was clearly seen.

[10] To determine the radial speed, angular width, and propagation direction of the CME, we applied a flux-rope model fit to SECCHI COR1 and COR2 and LASCO C2 and C3 images. The flux rope model used here is *Krall's and St. Cyr*'s [2006] flux rope model (hereafter KS06). The KS06 model is also called the elliptical flux rope model, which assumes that the flux rope has an elliptical axis with varying radial circular cross-section. The coordinate system used in the KS06 model has its origin at the CME eruption region on Sun's surface, the z-axis directed toward North, the x-axis directed toward West, and the y-axis directed along the Earth-Sun line, away from Earth. For simplicity, the separation distance between two flux-rope foot points has been neglected in the model. The geometry of the flux rope can be described by two parameters: the ratio of the semi-minor to semi-major axis of the ellipse $\lambda_\varepsilon = R_2/R_1$ and the axial aspect ratio $\Lambda_\alpha = 2R_1/d$, where R_1, R_2, and d are semi-major axis, semi-minor axis and width of the flux rope at its apex [cf. *Xie et al.*, 2009, Figure 1]. The orientation of the flux rope is defined by three angles: latitude λ, longitude ϕ, and tilt angle α, where the tilt angle is the rotation around its central axis. We used an iterative method to parameterize the flux rope model. First, we chose initial test parameters of the flux rope model based on the coronagraphic observations; we then iteratively adjusted the test parameters until the best fit of the flux rope model to both SECCHI and LASCO images were obtained by visual examination.

[11] Figure 3 shows the flux rope (FR) model fit for the CME; from left to right are COR1-A, C2, and COR1-B images superimposed with the flux rope model projected wireframe (yellow curves) at t = 09:50 UT, 10:55 UT and 09:50 UT, respectively. The model best-fit radial distances to SECCHI COR1/2 and LASCO C2/3 image frames at different times yield the height-time profile of the CME (Figure 4), $R_{tip}(t)$, where R_{tip} is the radial distance from the origin to the apex of the FR. The widths of the CME are given by: $\omega_{edge} = 2 \times tg^{-1}(0.5/\Lambda_\alpha)$, $\omega_{broad} = 2 \times tg^{-1}(\lambda_\epsilon)$, where ω_{edge} and ω_{broad} are the widths of the CME from edge-on and face-on views, respectively. For the April 3 CME, the fitting results gave that $R_1 = 0.8\ R_s$, $R_2 = 0.6\ R_s$, and $d = 2.0\ R_s$ at $R_{tip} = 2.6\ R_s$, where R_s is the solar radius, which yielded $\omega_{broad} = 74°$, and $\omega_{edge} = 64°$; the best-fit propagation direction of the CME are $(\lambda, \phi, \alpha) = (-23°, 3°, -70°)$. Comparison of our fit direction with previous studies

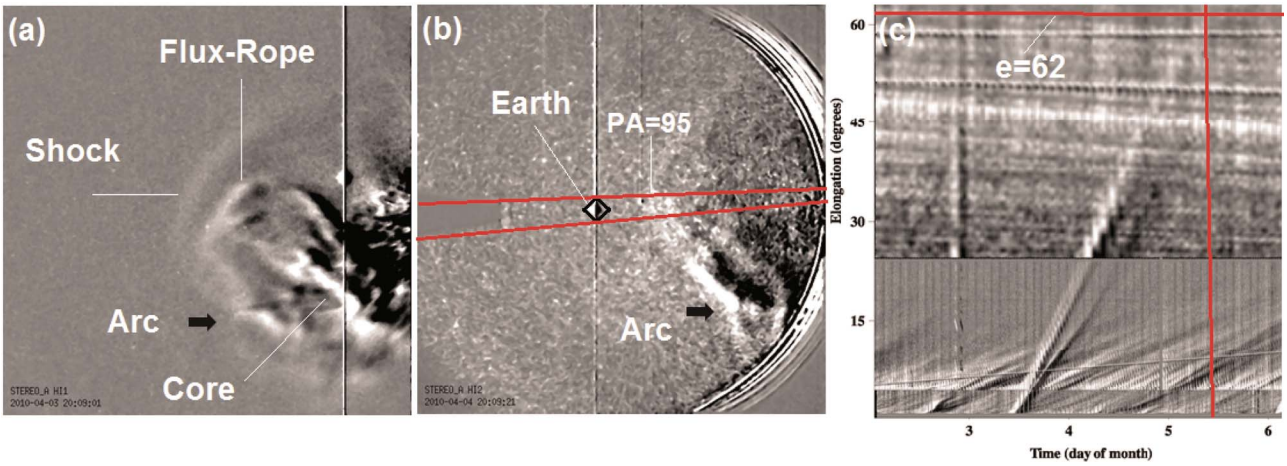

Figure 5. Running difference image of (a) HI1-A on April 3, 20:09 UT, (b) HI2-A image on April 4, 20:09 UT and (c) a time-elongation J-map along PA = 95°. Shock front, CME features and the Earth location are marked in the HI images. Thick arrows in Figures 5a and 5b denote the CME arc-like leading edge which has been indented. Two red lines in Figure 5b label the slit we use to make the Jmap at PA = 95°. The horizontal and vertical lines in the J-map mark the Earth position (at 62°) and the time (05:42 UT) when the shock arrived at Earth.

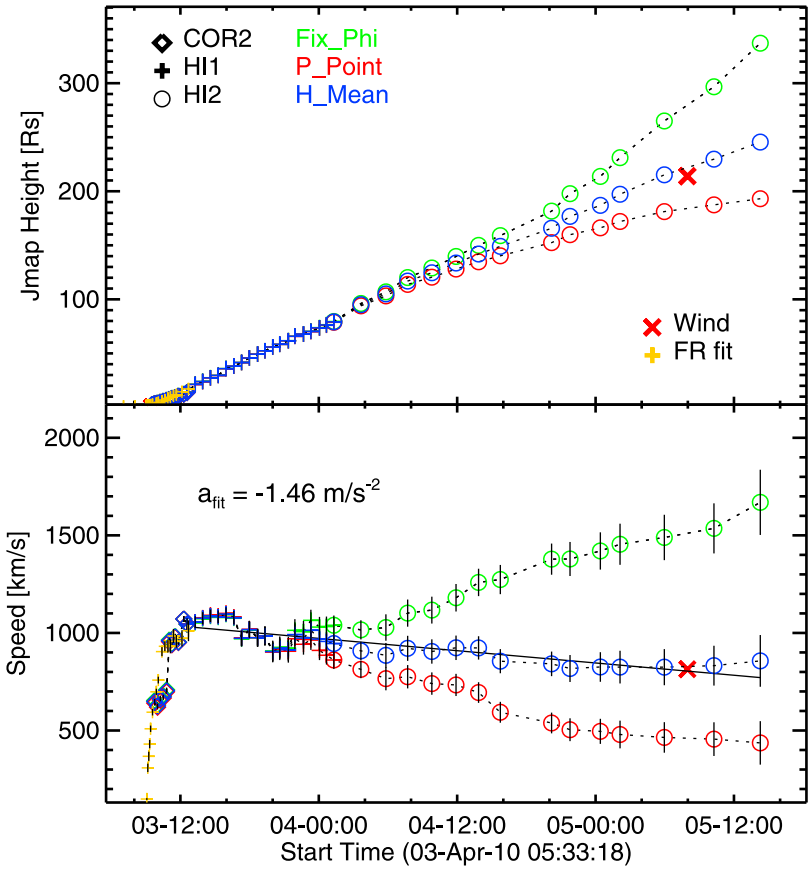

Figure 6. (top) Time-distance and (bottom) time-velocity profiles along the Sun-Earth line, for the three approximations denoted by red, green, and blue, respectively. The Fixed-ϕ method produces an apparent acceleration in HI2 FOV, while the Point-P method produces an apparent deceleration. The Harmonic Mean method yields the most plausible kinematic profile, with the smallest errors compared to the Wind observations.

shows that there is a very good agreement in longitude and decent agreement in latitude and tilt angle. The CME direction determined by *Möstl et al.* [2010] was S27° and W0°, and the direction determined by *Wood et al.* [2011] was S16°, W2° with tilt angle of −80°. Difference between Wood et al.'s (Möstl et al.) results and ours are 4° (7°), 3° (1°), 10°, respectively, in λ, ϕ, and α.

[12] Figure 4 shows the FR model fit height-time profile (solid line) and derived velocity (dashed line) over-plotted with the GOES X-ray flux (blue dotted line). The velocities are computed from adjacent data points of R_{tip} and the uncertainties in the computed velocity are estimated assuming the measurement uncertainty in distance ± 0.2 R_s at 15 R_s, i.e., the estimated fractional error in the distance is 1.3%. From the figure, we can see that the April 3 CME is accelerated from 268 km/s to 873 km/s rapidly within the COR1 FOV and its velocity reached a small peak around 10:05 UT, which is roughly the peak time of the X-ray flux, then accelerated gradually to 1011 km/s at ~12:08 UT. Note, however, that the resulting CME acceleration within the COR2 FOV should be taken cautiously since the maximum velocity uncertainty is ~150 km/s in the COR2 FOV, which is almost half as large as the velocity variation. Comparison of our CME velocity (1011 km/s) with those by *Möstl et al.* [2010] (990 km/s) and by *Wood et al.* [2011] (960 km/s) gives errors of 21 km/s and 51 km/s, respectively. These errors fall within the maximum velocity uncertainty range.

2.3. Kinematic Analysis With J-maps

[13] With the help of J-maps constructed from COR2, HI1 and HI2 images, we can derive the CME trajectory in the heliosphere from near the Sun all the way to 1 AU [*Wood et al.*, 2010]. Three methods have been generally used to infer radial distances, r, from the measured elongation angles, ϵ, from white light images: (1) Point-P [*Howard et al.*, 2006]; (2) Fixed-ϕ [*Kahler and Webb*, 2007; *Wood et al.*, 2010]; and (3) Harmonic Mean [*Lugaz et al.*, 2009]. The Point-P method assumes a broad spherical front centered at the Sun, and r and ϵ are related by: $r = d\sin\epsilon$, where d is the distance from the spacecraft to the Sun. The Fixed-ϕ method assumes a very narrow CME traveling with fixed direction with: $r = d\sin\epsilon/\sin(\epsilon + \phi)$, where ϕ is the angle between the CME trajectory and the line of sight (LOS) from the observer to the Sun. The Harmonic Mean method approximates the CME as a sphere centered halfway between the Sun and the CME's leading edge, and yields a CME radial distance given by: $r = 2d\sin\epsilon/(1 + \sin(\epsilon + \phi))$,

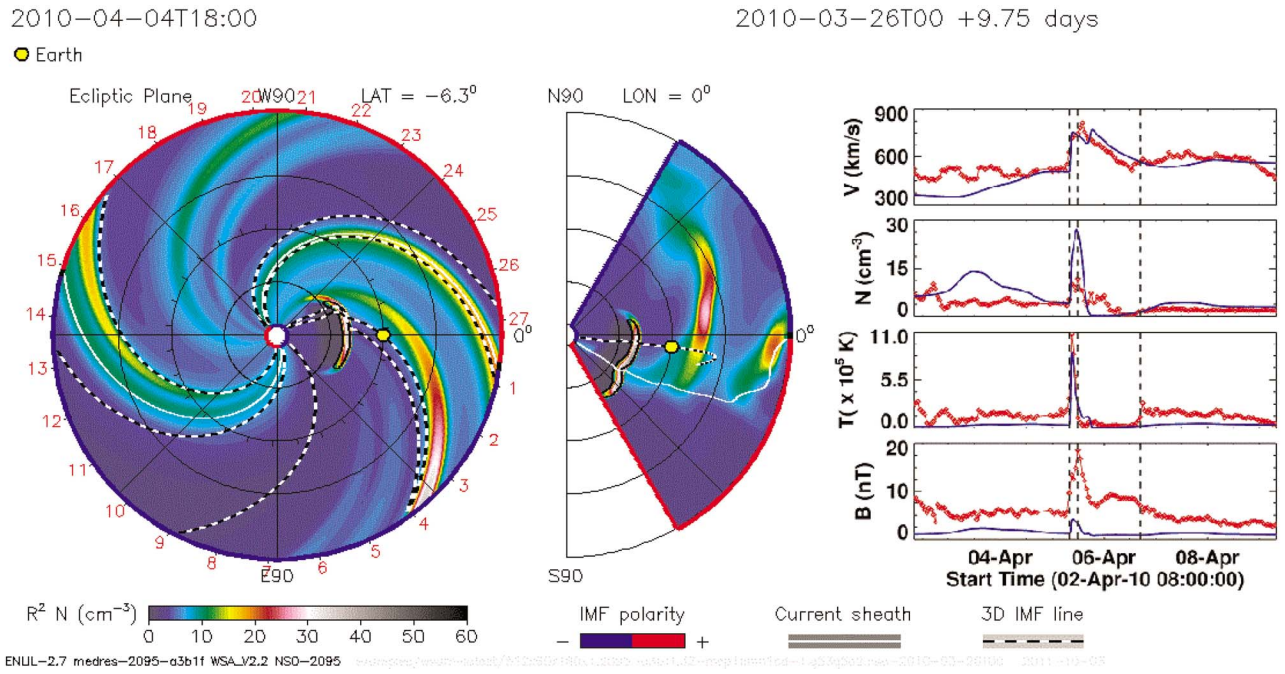

Figure 7. Simulation results of 2D density contours in the (left) ecliptic plane and (middle) meridian plane on April 4, 18:00 UT. The density in the simulation is normalized for an r^{-2} falloff with distance. (right) The comparison of the simulated (blue solid lines) and observed Wind solar wind plasma and magnetic field data (red dotted lines) at 1 AU between April 2 and 9.

which is the harmonic average of the Point-P and the Fixed-ϕ approximations.

[14] We show in Figure 5, from left to right, running difference images of HI1-A, HI2-A, and a time-elongation J-map along the Sun-Earth line with PA = 95°, where PA is the position angle measured counterclockwise from the north. Figure 5a shows three features of the propagating CME: the southward ejecta (flux rope); the shock front with faint and sharp brightness enhancements, extending much wider in latitude than ejecta; and the core at rear of the flux rope. Note that there was a deformation at the shock front along the CME central leading edge (LE; hereafter LE denotes the leading edge of the CME at its central axis) due to the interaction between the CME and the streamer ahead of it. The Wilcox Solar Observatory (WSO)source surface synoptic charts (R = 2.5 radial model) (http://wso.stanford.edu/synsourcel.html) indicated that the location of the current sheet (streamer belt neutral line) was ∼S23° on Apr 2–3, 2010, just ahead of the CME LE. The streamer was marked by arrows in the COR1 and COR2 images (Figure 2). The CME/shock front was interacting with and indented by the streamer; an arc-like front formed, as marked by thick arrows in Figures 5a and 5b. The heliocentric distances of the shock along the Sun-Earth line and the LE on April 3, 20:09 UT are ∼56 R_s and ∼49 R_s, respectively. In Figure 5b, when the CME propagated farther out into the HI2-A FOV, the shock sheath and the flux rope ejecta along the LE had been compressed together and we can only see one complex compressed front. The ejecta along the Sun-Earth line is too faint to see due to the further expansion.

[15] Figure 6 (top) shows a time-distance $r(t)$ plot of the shock along the Sun-Earth line with PA = 95°, where distances are derived from elongation angles in the J-map using the three methods discussed above. We used the CME direction ϕ = 75° with respect to STA (i.e., E8° with respect to Earth) for the Fixed-ϕ and Harmonic Mean approximations. The direction was chosen so that $r(t)$ matched best with both the FR model fit results and the observed SAT at Wind. Figure 6 (bottom) is the inferred velocity of the shock. Here we omitted some distance points (6 points in this case) instead of using adjacent data points to compute velocities to avoid large errors caused by distance measurement errors. The velocity uncertainties are estimated assuming 1%, 2% and 3% fractional errors in the distance measurements for COR2, HI1 and HI2, respectively, the same given by *Wood et al.* [2010].

[16] We found that the three approximations yield similar profiles within the COR2 and HI1 FOV, but not in the HI2 FOV. The Point-P approximation produced a dramatic deceleration, while the Fixed-ϕ approximation produced a large acceleration. These are apparent accelerations and caused by the apparent leading edges seen by HI. Due to a projection effect and the CME angular width as it expands, the actual LE of the CME is not seen by HI but the far-side or nearside flank of the CME, resulting in artificial distance increases and decreases [cf. *Wood et al.*, 2010, Figure 4]. Among three approximations, the Harmonic Mean method yields a more plausible kinematic profile. Compared to the Wind SAT and in situ plasma bulk velocity in the sheath, marked by red "X" symbols in Figure 6, the Harmonic Mean method gives the smallest errors of ∼2 hours and ∼50 km/s, respectively. Note that there is an overlap of distances from the J-map and the flux rope model fit in COR2, denoted by

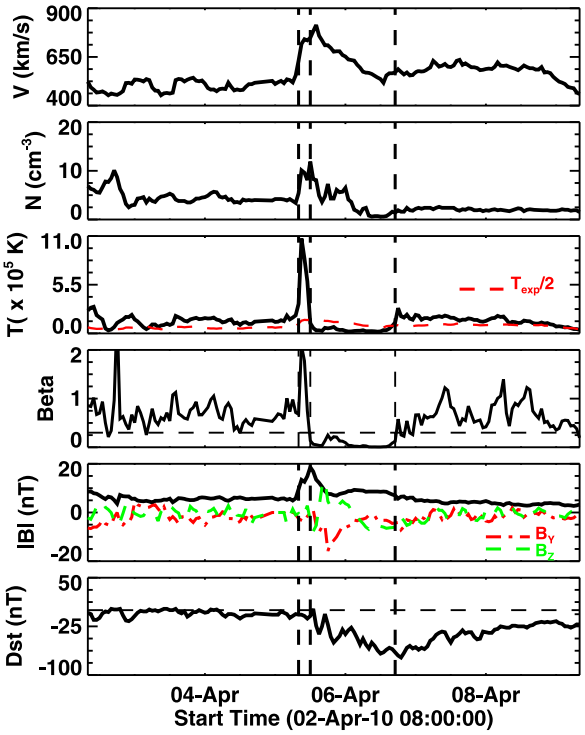

Figure 8. Solar wind plasma and magnetic field data (Wind). From top to bottom: proton bulk velocity V, proton number density N, proton temperature T, plasma β, magnetic field magnitude $|B|$ and components B_y and B_z, and Dst index. The three vertical dashed lines indicate the shock arrival and the ICME interval, where the ICME is identified by the interval that shows proton temperature depression below half the expected solar wind temperature T_{exp}. The horizontal lines in β and D_{st} are lines for $\beta = 0.3$ and $D_{st} = 0$, respectively.

orange plus symbols in the figure. These two distances are shown to be consistent with each other.

3. Simulation With Numerical Heliospheric Model

[17] To fully investigate the three-dimensional (3D) evolution and formation of the CME-driven shock in the inner heliosphere, we used the WSA-Cone-ENLIL model. The WSA-Cone-ENLIL model [e.g., *Odstrčil et al.*, 1996; *Odstrcil and Pizzo*, 1999; *Odstrcil et al.*, 2005] is well-known in the solar-helio community, and ENLIL version 2.3a is currently available to users at the Community Coordinated Modeling Center (CCMC). ENLIL is a time-dependent 3D MHD model of the heliosphere, and it solves for plasma mass, momentum and energy density, as well as magnetic field, using a Total-Variation-Diminishing Lax-Friedrich (TVDLF) algorithm [*Toth and Odstrcil*, 1996]. Its inner radial boundary is located beyond the sonic point, typically at 21.5 R_s (or 0.1 AU) for WSA (30 R_s for MAS), and the outer boundary is set at 2.0 AU. In the simulation spherical coordinates are used, and the three independent spatial variables are the radial position r, the meridional (latitude) angle θ, and the azimuthal (longitude) angle ϕ. The meridional and azimuthal extents span 30°–150° and 0°–360°, respectively. The computational region has 512 × 60 × 180 grid points, and the uniform spacing of computational grid points are $\Delta r = 0.794\ R_s$, $\Delta\theta = 2°$, and $\Delta\phi = 2°$.

[18] The CME is input into the ENLIL simulation domain as a hydrodynamic spherical cloud. This ejecta has a uniform velocity and diameter corresponding to the fitted radial CME speed and width. Parameters describing the CME's geometry and kinematics, such as size, speed and direction, can be obtained by fitting the cone model (or other forward-modeling techniques, e.g. flux rope model) to coronagraph observations [e.g., *Xie et al.*, 2004, 2009; *Krall and St. Cyr*, 2006; *Thernisien et al.*, 2006]. Further, the model assumes that the ejecta density has the density four times larger than the mean value in the fast stream and the same temperature as in the fast stream. It is assumed that the momentum flow and thermal pressure are constant at the inner boundary (0.1 AU) and that the density and temperature in the fast stream is 250 cm^{-3} and 0.8 MK, respectively. The input values were chosen by matching the simulated properties of the shock upstream reasonable well with in situ measurements at 1AU.

[19] The numerical simulation is done in two stages: 1) setup the background solar wind based on the Wang-Sheeley-Arge (WSA) [e.g., *Arge and Pizzo*, 2000; *Arge et al.*, 2004] or MAS [e.g., *Linker et al.*, 1999; *Riley et al.*, 2001] models; 2) insert a CME propagating in that background at the time when the observed CME passes the inner boundary (which is usually at 21.5 R_s for WSA). In the simulation, we used the flux rope model fit results of actual speed (1011 km/s), face-on half angular width (37°), and direction (described in Section 2.2) as input parameters of the CME. The background solar wind was set up using the WSA model with photospheric magnetograms from the National Solar Observatory's (NSO) Global Oscillation Network Group (GONG) system, and the CME was launched into the computational heliospheric domain at the inner boundary 21.5 R_s at t = 13:29 UT.

4. Simulation Results

4.1. Comparison of the Simulation Results With In-Situ Observations

[20] Figure 7 shows the simulated density in the ecliptic plane (left) and meridian plane (middle) as two-dimensional (2D) density contours on April 4 at 18:00 UT (movies are available online at http://ccmc.gsfc.nasa.gov/database_SH/h_xie_100311_SH_1.php and in the auxiliary material). In the figure W (West) is up and E (East) is down in the ecliptic plane (left panel); and N (North) is up and S (South) is down in the meridian plane (middle panel). The Sun-Earth line is roughly horizontal with the Earth to the right. The heliographic location of the Earth is S6.3W00, i.e., in the center of the ecliptic plane and slightly southward in the meridian plane, as marked by yellow filled circles. The 2D density contours show that the CME has encountered two slow, dense streamers: one is located at the west flank of the CME and another is located at the center of the CME along the LE. The interaction between the CME and the dense streamers and the ambient solar wind has led to the formation of an arc-like structure at the CME LE (middle panel) and caused the IMF (black-white dashed line) to be deflected (left panel). Figure 7 (right) shows the simulated (blue solid lines)

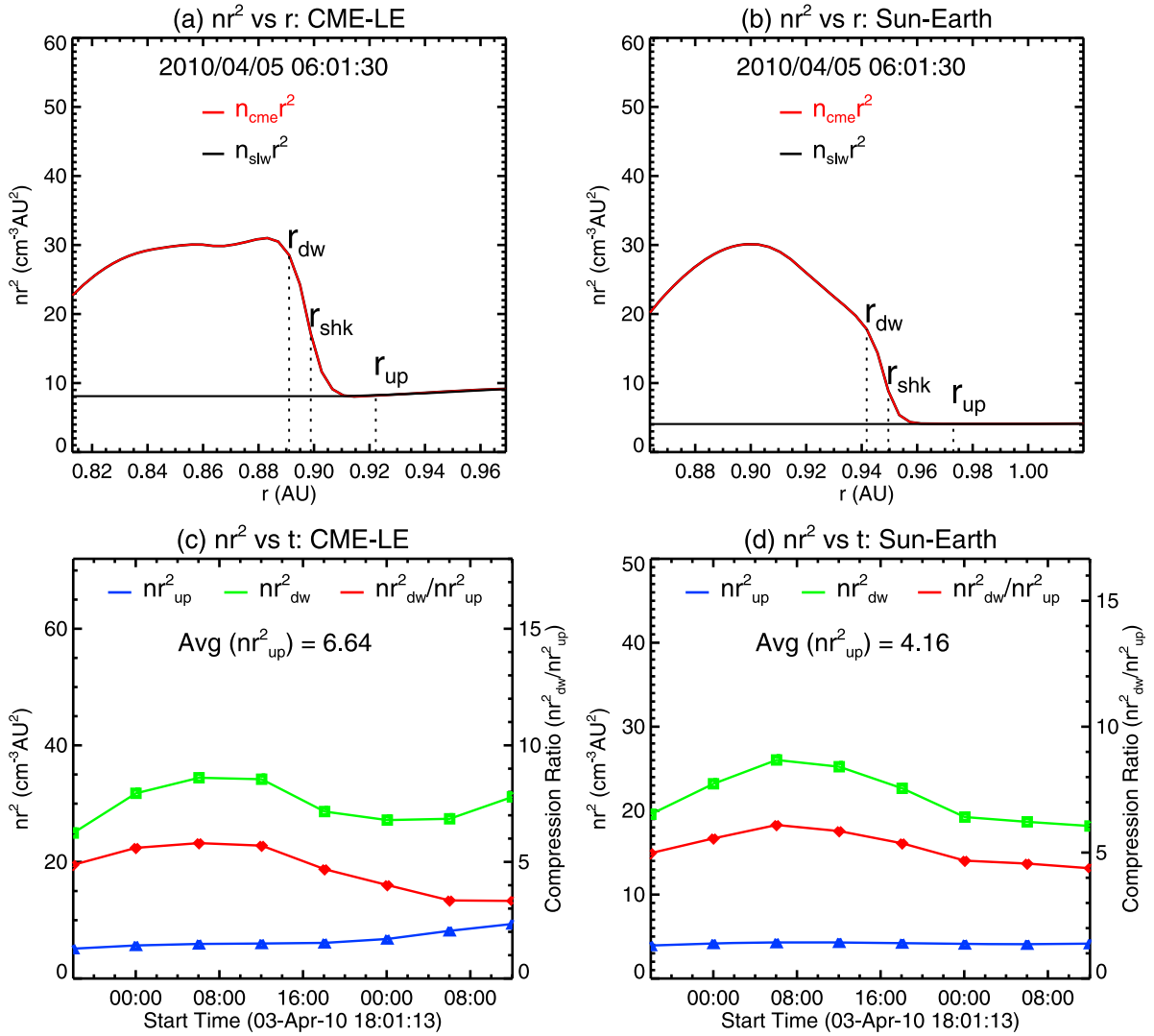

Figure 9. (left) Simulation results of nr^2 (density times square of radial distance) as function of distance r: (a) along the LE propagation direction; (b) along the Sun- Earth line on April 5, 06:01:30 UT, where red and black lines denote the CME and ambient solar wind plasma density, respectively, and three dashed vertical lines mark locations of the shock front, upstream and downstream. (right) nr^2_{up}, nr^2_{dw}, shock compression ratio nr^2_{dw}/nr^2_{up} as function of time (c) along the LE and (d) along the Sun-Earth line.

and the observed Wind solar wind plasma and magnetic field data (red dotted lines) at 1 AU between April 2 and 9. The IP shock arrived at Wind on April 5 at 07:58 UT, followed by an ICME from April 5 at 12:00 UT to April 6 at 17:00 UT. Figure 8 is the in situ Wind observation data plus the Dst index. From Figure 8, we can see that the long-duration geomagnetic storm was first caused by a negative B_y with a peak of ~ -16 nT on Apr 5, 18:00 UT, and then enhanced farther by long-duration negative B_z and B_y of ~ -7 nT. The observed ICME has a smooth magnetic rotation and enhanced magnetic strength $|B|$, low proton temperature T and plasma β, and a declining velocity V profile (due to the ICME expansion in the solar wind). However, it cannot be fitted to any magnetic cloud models [cf., *Möstl et al.*, 2010] because the ICME was southward directed (S25W03) and only its northern flank passed over Earth.

[21] The ENLIL model predicted the shock arrival at Earth at 08:57 UT on April 5, with an error of $\sim$1.0 hour compared to the Wind SAT of 07:58 UT. Thus the ENLIL model provided a good prediction of the SAT for this event. Note that, however, the model requires the CME density and temperature as input at 0.1 AU which are not direct measurements, thus adding a degree of uncertainty. We have performed runs by assuming that the CME has the density either four times or twice larger than the fast stream value, and it yields a variation in SAT (shock arrival time) of $\sim$7 hrs. Furthermore, since the ENLIL ejecta is a pure hydrodynamic structure, the absence of the CME internal magnetic structure has caused the model to overestimate plasma density N and temperature T, and to underestimate total B field of the ICME.

4.2. Comparison of the Simulation Results With J-maps

[22] In order to study the evolution of the IP shock driven by the CME, we need to find the locations of the shock front

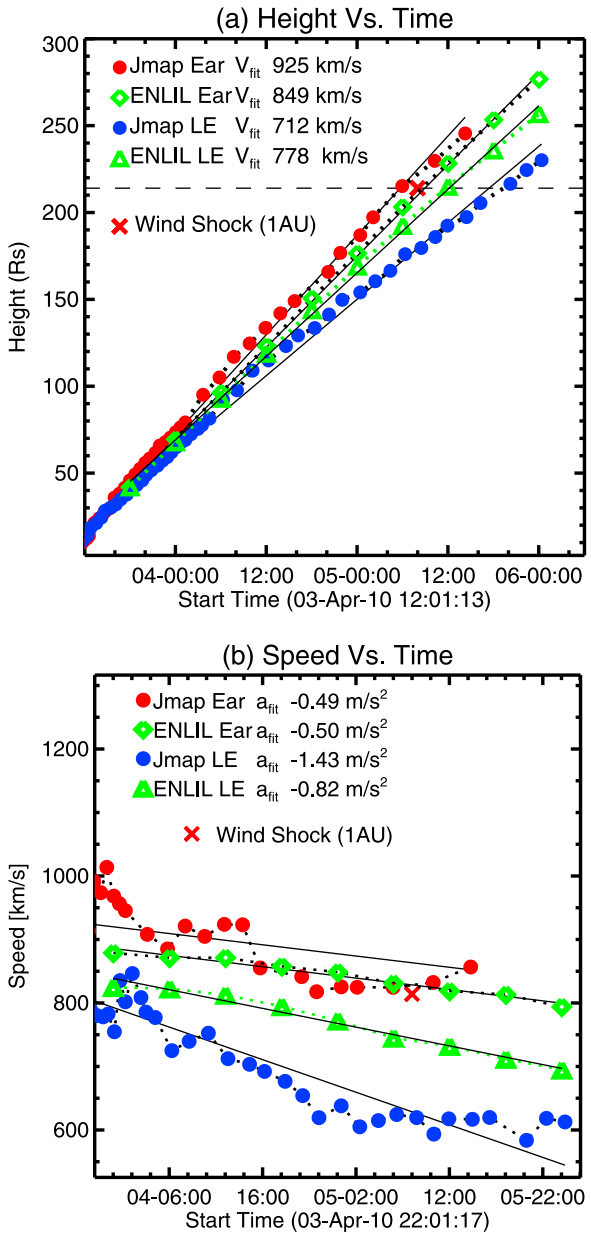

Figure 10. Comparison of (a) time-distance and (b) time-velocity profiles of the shock from the ENLIL model and J-maps, where V_{fit} and a_{fit} are the linear-fit velocity and acceleration.

where the sudden increase of density (or velocity) occurs. Figure 9 (left) shows an example of how to locate the simulated shock, where we plot density times the square of radial distance nr^2 as function of distance r (a) along the LE propagation direction; (b) along the Sun-Earth line on April 5 at 06:01 UT. In Figures 9a and 9b, locations of the shock front, upstream and downstream are marked by three vertical lines r_{sk}, r_{up}, and r_{dw}. We define a shock front r_{sk} by locating the largest slope of nr^2, i.e. largest $d(nr^2)/dr$. The shock downstream is defined as $r_{dw} = r_{sk} - 2$ spacing grids because the average thickness of the shock is ~4 spacing grids due to the limitation of the 3D code resolution. We choose the shock upstream r_{up} to be $r_{sk} + 5$ spacing grids to ensure that the selected upstream has fallen into the smooth ambient solar wind region, where nr^2_{up} remains nearly constant.

[23] Figure 9 (right) plots the upstream density nr^2_{up}, the downstream density nr^2_{dw}, and the shock compression ratio nr^2_{dw}/nr^2_{up} as function of time: along the LE propagation direction (Figure 9c) and along the Sun-Earth line (Figure 9d). Comparing Figures 9c and 9d, we can see that the shock compression ratios along two propagation directions have similar trends. Both curves experience an initial increase and then gradually decrease. The compression ratio along the LE (Sun-Earth) propagation direction reaches a maximum value of 5.81 (6.10) on April 4, 06:03 UT. The background solar wind density, nr^2_{up}, remains nearly constant along the Sun-Earth line and slightly increases along the LE propagation direction, due to the slow dense streamer ahead of the CME. The mean values of the solar wind density along the LE and Sun-Earth are 6.64 cm^{-3} and 4.16 cm^{-3}, respectively. We apply these values to the kmTII method in Section 5. Note that the maximum compression ratios along the both LE and Sun-Earth propagation directions are greater than the theoretical threshold of 4 [*Priest*, 1982]. This is due to a limitation of the 3D code resolution producing the shock front thickness to be too large (the spacing of grids) [*Steinolfson et al.*, 1975].

[24] Figure 10a compares the simulated time-distance profiles of the shock along the LE and Sun-Earth line with the time-distance profiles from J-maps along the LE and Sun-Earth line. All the distances in the figure are measured for the shock front. We found that the shock propagation along the LE propagation direction lagged behind the one along the Sun-Earth line in both the ENLIL model and J-map, due to the interaction between the CME and the streamer at the LE. HI2-A movies (see auxiliary material) clearly show that the shock front has been flattened and compressed and the Earthward shock front (a faint brightness enhancement) arrived earlier at 1 AU than the shock front along the LE.

[25] The shock arrival times along the LE and Sun-Earth line are 12:10 UT and 08:57 UT in the ENLIL model; and 17:27 UT and 05:42 UT in the J-map (all these times refer to April 5). The linear-fit shock velocities along the LE and Sun-Earth line are 778 km/s and 849 km/s in the ENLIL model; and 712 km/s and 925 km/s in the J-map. The differences in SAT between the ENLIL model and J-map are ~5 hours along the LE, and ~−3 hours along the Sun-Earth line. The differences in linear shock speed between the ENLIL model and J-map are 66 km/s along the LE, and ~−76 km/s along the Sun-Earth line. Thus the simulation results agree with the observations within the error range of the measurements. The simulation reproduced the overall dynamics of the shock propagation with realistic large scale structures.

[26] Note that the difference between the two propagation directions for the shock, in the ENLIL model, is much smaller than that in the J-map. The differences in SAT and shock speed in the ENLIL model are ~3 hours and 71 km/s between the two directions; and 11.5 hours and 213 km/s in the J-map. We will discuss this in Section 6.

[27] Figure 10b shows the time-velocity profiles of the CME inferred from the distances in Figure 10a. All four velocity profiles show small decelerations. The linear-fit decelerations along the Sun-Earth line are similar, with

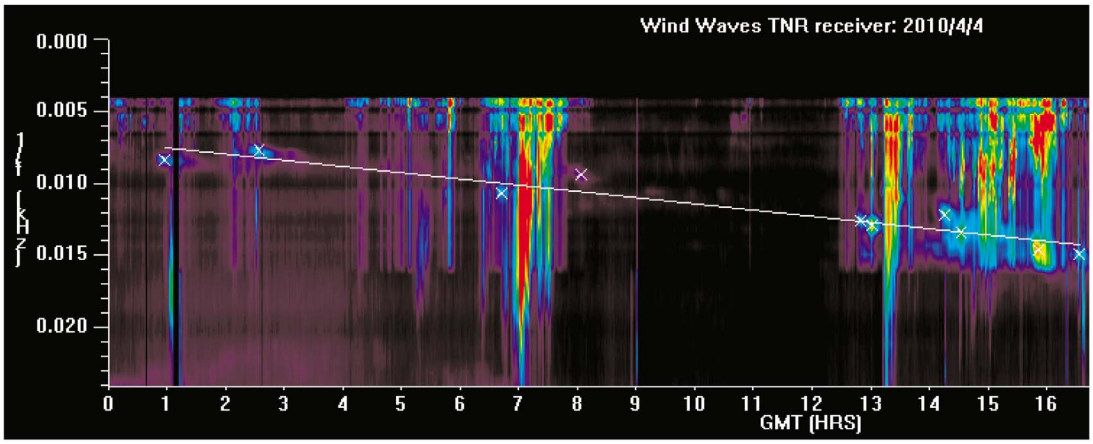

Figure 11. The kmTII dynamic spectrum detected by the TNR receiver on April 4 2010. Note the scale of the vertical axis is in units of 1/f. "X" symbols in the figure mark the selected data points in the spectrum.

values of -0.49 and -0.50 m/s^2 in the ENLIL model and J-map, respectively. But the linear-fit deceleration in the ENLIL model is smaller (-0.82 m/s^2) than that (-1.43 m/s^2) in the J-map along the LE. The deceleration from the J-map along the LE is consistent with the IP acceleration $a = 2.193 - 0.0054\ u$ from *Gopalswamy et al.*'s [2005b] empirical shock arrival (ESA) model, where u is the CME speed. For $u = 712$ km/s; $a = -1.65$ m/s^2. The ESA model gives an SAT of 15:30 UT for an earthward speed of 925 km/s, which gives an error of ~7.5 hours.

5. The "kmTII" Technique

[28] For the April 3, 2010 CME, no decameter-hectometric (DH) type II radio burst was detected. But a kilometric type II (kmTII) radio burst starting from April 4 00:58 to 16:33 UT was detected by Wind/WAVES. Such events are generally rare and have a relatively slower average speed compared to other CMEs with radio-loud shocks as discussed by *Gopalswamy et al.* [2010]. Figure 11 shows the dynamic spectrum of the kmTII radio burst recorded by the TNR receiver on April 4, 2010. Note the scale of the vertical axis is in units of 1/f. The solid line represents the linear fit of the drifting 1/f as a function of time. Using a simple density model in which $n = n_0/r^2$ (n_0 is the plasma density at 1 AU in units of cm^{-3}) [e.g., *Leblanc et al.*, 1998], the time-distance profile of the CME-driven shock can then be obtained from the frequency drift given by $r(t) = a\sqrt{n_0}/f(t)$, where $r(t)$ is the heliocentric distance where the kmTII occurs in units of AU, $f(t)$ is the drifting frequency in units of kHz, and $a = 9$ or 18 is a constant for fundamental or harmonic emission, respectively. The derived shock speed is $V_{sh} = a\sqrt{n_0} \times \frac{d}{dt}(1/f) \times 1.5 \times 10^8$ (km/s) [*Reiner et al.*, 1998]. Figure 12 plots the time-distance profile of the shock propagation inferred from the kmTII method, superimposed with trajectories extracted from the J-maps. Open circles represent data points extracted from the J-maps along the LE (blue) and the Sun-Earth line (red), and green diamonds represent the results derived from the kmTII method using the ENLIL model density (a) at Earth $n_0 = 4.16$ cm^{-3} and (b) at the LE $n_0 = 6.64$ cm^{-3} in Figure 9. In Figure 12a, assuming that the kmTII occurs near the Sun-Earth line, the kmTII estimated linear shock speed is 656 km/s and the estimated SAT is 22:57 UT, yielding errors of ~15 hours and 269 km/s, compared to the Wind SAT of 07:58 UT and the J-map Earthward shock speed of 925 km/s. In Figure 12b, the kmTII is assumed to occur near the shock at the LE. The kmTII prediction gives a linear-fit shock speed of 829 km/s and the predicted SAT is 09:44 UT, yielding errors of ~2 hours and 96 km/s, compared to the Wind SAT and the J-map Earthward shock speed. Thus applying the plasma density value near the LE has improved the kmTII prediction error from 15 hours to 2 hours, and the kmTII prediction accuracy largely relies on the value of the plasma density it used. Table 1 summarizes the derived shock propagation characteristics from the ENLIL simulation, J-maps, and kmTII method.

6. Discussion and Conclusion

[29] We have comprehensively investigated the evolution and propagation of the April 3, 2010 CME-driven shock, combining STEREO and SOHO white light observations, kilometric type II radio data with the simulation using the WSA-Cone-ENLIL model. We used the KS06 flux rope model fit to SECCHI and LASCO observations to determine the CME speed, size and direction, as well as its time-distance profile when the CME is within the C3 FOV. We derived the time-distance profile of the CME/shock in the heliosphere from the J-maps constructed from SECCHI images, from near the Sun all the way to 1 AU. The shock front was seen clearly in the HI1-A images staring from April 3 ~ 15:29 UT. Three methods, i.e., P-Point, Fixed-ϕ, and Harmonic Mean, were used to derive the radial distances from elongation angles in the J-maps. The obtained results show that the harmonic mean approximation gives the best results for the time-distance and time-velocity profiles of the shock, yielding the smallest errors compared to the Wind observations of the shock arrival time and in situ plasma bulk velocity in the sheath. To fully investigate the formation and evolution of the shock and predict the shock arrival time, we used the WSA-Cone-ENLIL model simulation and the kmTII technique. The kinematic analysis from J-maps together with in-situ data provided us with a

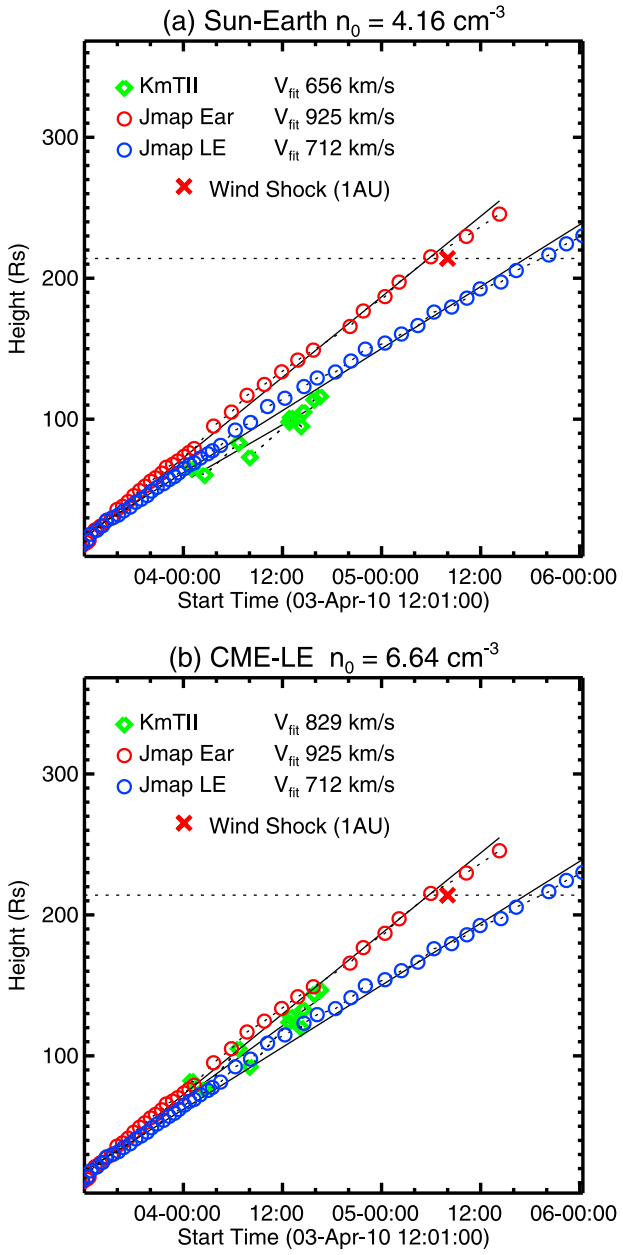

Figure 12. Comparison of the time-distance profiles of the shock from J-maps and kmTII with (a) n_0 = 4.16 cm^{-3} along the Sun-Earth line and (b) n_0 = 6.64 cm^{-3} along the CME LE.

valuable opportunity to validate the simulated results and the kmTII prediction.

[30] We found that the ENLIL model provided good predictions on the shock arrival time along both the Sun-Earth line and the CME-LE propagation directions. The ENLIL model predicted the SAT at Earth on April 5 at 08:57 UT and the SAT at 1AU along the LE of ~12:10 UT with ~1 ± 7 hours and ~5 ± 7 hours errors, respectively, compared to the Wind SAT and J-map SAT along the LE. It also reproduced the overall dynamics of the shock propagation with realistic large scale structures in the simulation, including the background solar wind density along the Sun-Earth line, the locations of streamer outflows, the CME-streamer interaction, and the flattened arc-like shock front along the LE.

[31] The kmTII prediction largely relies on the coronal density model and the electron density n_0 at 1 AU, which is assumed to be the average solar wind value 7.2 cm^{-3} by *Cremades et al.* [2007]. To investigate the possibility of using the ENLIL model density to improve the kmTII prediction, we applied the solar wind density obtained from the simulation to the kmTII method. With n_0 = 4.16 cm^{-3} at Earth and n_0 = 6.64 cm^{-3} at the LE, the estimated shock speeds are 656 km/s and 829 km/s, yielding SATs of 22:57 UT and 09:44 UT and errors of ~15 hours and ~2 hours, compared to the Wind SAT of 07:58 UT.

[32] Note that, however, the good prediction of ~2 hours was due to the cancelation of two errors, i.e., the error in the location where the kmTII occurred and the density error from the simulation. First, the kmTII radio emission was assumed to occur at the CME LE, where the shock had been intensified due to the CME-streamer interaction and low Alfvén speed (high density) in the streamer, as shown in Figure 9a. Second, the actual error is ~7.7 hours when compared to the J-map SAT of 17:27 UT at the LE, indicating the ENLIL model had overestimated the density along the LE, resulting in a smaller SAT, which yielded a small error of ~2 hours (compared with 07:58 UT).

[33] One possible reason for the ENLIL model's overestimating the plasma density along the LE may be because the simulation didn't reproduce the small flux-rope like V-shaped structure which is observed by HI-A. On closer examination of HI-A image movie, we see that a small flux-rope like V-shaped structure was formed out of the streamer outflow ahead of the CME LE. The first appearance time of this small FR-like V-shaped structure in HI1-A was around April 3 20:09 UT. Its formation was likely due to reconnection of magnetic field lines at the tip of helmet streamers [e.g., *Rouillard et al.*, 2010]. This V-shaped structure was observed to be entrained by the streamer outflows and

Table 1. Summary of the Predicted Shock Properties From the Simulation, J-maps, and kmTII Method

	ENLIL		J-map		kmTII	
	Sun-Earth	CME-LE	Sun-Earth	CME-LE	Sun-Earth n_0(4.16) (cm^{-3})	CME-LE n_0(6.64) (cm^{-3})
SAT (UT)[a]	08:57	12:10	05:42	17:27	22:57	09:44
V_{fit} (km s^{-1})[b]	849	778	925	712	656	829
a_{fit} (m s^{-2})[c]	−0.50	−0.82	−0.49	−1.43	—	—

[a]Shock arrival time; all times are on April 5.
[b]Shock linear-fit velocity.
[c]Shock linear-fit acceleration.

traveling with the similar speed as the solar wind. The CME caught up with the V-shaped structure at ~02:09 UT on April 4, as shown in HI2-A image movie, and then merged together around ~20:09 UT. An arc-like shaped front was formed due to the large compression caused by the interaction of the CMEs in the HI2-A movie. This interacting duration was consistent with the time period when the kilometer type II burst occurred, suggesting that the CME-streamer (or CME-CME) interaction enhanced the shock intensity and produced the type II radio burst [e.g., *Gopalswamy et al.*, 2001]. Since the ENLIL model didn't include the CME's internal magnetic field, it didn't reproduce the V-shaped FR-like structure formed out of the streamer. This may explain why the simulation results didn't reproduce as big of a difference of the shock along two propagation directions, i.e., the LE and the Sun-Earth line, as that shown in the J-map. It may also explain why the ENLIL model produced too large of a plasma density upstream of the shock in order to compensate the magnetic field pressure from the small FR-like CME along the LE. If a CME-driven shock occurs in a background solar wind which is more homogeneous, using the ENLIL model has the potential to improve the kmTII prediction. In turn, the kmTII observations can constrain and help improve the future modeling of shocks.

[34] **Acknowledgments.** The authors would like to thank the support of STEREO, SOHO, WIND teams. The STEREO SECCHI data are produced by a consortium of RAL (UK), NRL (USA), LMSAL (USA), GSFC (USA), MPS (Germany), CSL (Belgium), IOTA (France), and IAS (France). The SOHO LASCO data are produced by a consortium of the Naval Research Laboratory (USA), Max-Planck-Institut für Aeronomie (Germany), Laboratoire d'Astronomie (France), and the University of Birmingham (UK). We acknowledge magnetogram data from NSO/GONG (Global Oscillation Network Group) and the WIND data from NASA's Space Physics Data Facility. This work was supported by NASA LWS TR&T program (08-LWSTRT08-0029). H. C. is member of Carrera del Investigador Científico, CONICET. M. L. Mays acknowledges support from an appointment to the NASA Postdoctoral Program at Goddard Space Flight Center, administered by Oak Ridge Associated Universities through a contract with NASA.

[35] Philippa Browning thanks the reviewers for their assistance in evaluating this paper.

References

Arge, C. N., and V. J. Pizzo (2000), Improvement in the prediction of solar wind conditions using near-real time solar magnetic field updates, *J. Geophys. Res.*, *105*, 10,465–10,480.

Arge, C. N., J. G. Luhmann, D. Odstrcil, C. J. Schrijver, and Y. Li (2004), Stream structure and coronal sources of the solar wind during the May 12th, 1997 CME, *J. Atmos. Sol. Terr. Phys.*, *66*, 1295–1309.

Bougeret, J.-L., et al. (1995), Waves: The radio and plasma wave investigation on the Wind spacecraft, *Space Sci. Rev.*, *71*, 231–263, doi:10.1007/BF00751331.

Bougeret, J. L., et al. (2008), S/WAVES: The radio and plasma wave investigation on the STEREO mission, *Space Sci. Rev.*, *136*, 487–528, doi:10.1007/s11214–007–9298–8.

Brueckner, G. E., et al. (1995), The Large Angle Spectroscopic Coronagraph (LASCO), *Solar Phys.*, *162*, 357–402, doi:10.1007/BF00733434.

Cremades, H., O. St. Cyr, and M. Kaiser (2007), A tool to improve space weather forecasts: Kilometric radio emissions from Wind/WAVES, *Space Weather*, *5*, S08001, doi:10.1029/2007SW000314.

Eyles, C. J., et al. (2009), The heliospheric imagers onboard the STEREO mission, *Solar Phys.*, *254*, 387–445, doi:10.1007/s11207–008–9299–0.

Gopalswamy, N., S. Yashiro, M. L. Kaiser, R. A. Howard, and J.-L. Bougeret (2001), Radio signatures of coronal mass ejection interaction: Coronal mass ejection cannibalism?, *Astrophys. J.*, *548*, L91–L94, doi:10.1086/318939.

Gopalswamy, N., E. Aguilar-Rodriguez, S. Yashiro, S. Nunes, M. L. Kaiser, and R. A. Howard (2005a), Type II radio bursts and energetic solar eruptions, *J. Geophys. Res.*, *110*, A12S07, doi:10.1029/2005JA011158.

Gopalswamy, N., A. Lara, P. K. Manoharan, and R. A. Howard (2005b), An empirical model to predict the 1-AU arrival of interplanetary shocks, *Adv. Space Res.*, *36*, 2289–2294, doi:10.1016/j.asr.2004.07.014.

Gopalswamy, N., H. Xie, P. Mäkelä, S. Akiyama, S. Yashiro, M. L. Kaiser, R. A. Howard, and J.-L. Bougeret (2010), Interplanetary shocks lacking Type II radio bursts, *Astrophys. J.*, *710*, 1111–1126, doi:10.1088/0004–637X/710/2/1111.

Howard, T. A., D. F. Webb, S. J. Tappin, D. R. Mizuno, and J. C. Johnston (2006), Tracking halo coronal mass ejections from 0–1 AU and space weather forecasting using the Solar Mass Ejection Imager (SMEI), *J. Geophys. Res.*, *111*, A04105, doi:10.1029/2005JA011349.

Kahler, S. W., and D. F. Webb (2007), V arc interplanetary coronal mass ejections observed with the Solar Mass Ejection Imager, *J. Geophys. Res.*, *112*, A09103, doi:10.1029/2007JA012358.

Kaiser, M. L., T. A. Kucera, J. M. Davila, O. C. St. Cyr, M. Guhathakurta, and E. Christian (2008), The STEREO mission: An introduction, *Space Sci. Rev.*, *136*, 5–16.

Krall, J., and O. C. St. Cyr (2006), Flux-rope coronal mass ejection geometry and its relation to observed morphology, *Astrophys. J.*, *652*, 1740–1746, doi:10.1086/508337.

Leblanc, Y., G. A. Dulk, and J.-L. Bougeret (1998), Tracing the electron density from the corona to 1 AU, *Solar Phys.*, *183*, 165–180.

Linker, J. A., Z. Mikić, D. A. Biesecker, R. J. Forsyth, S. E. Gibson, A. J. Lazarus, A. Lecinski, P. Riley, A. Szabo, and B. J. Thompson (1999), Magnetohydrodynamic modeling of the solar corona during Whole Sun Month, *J. Geophys. Res.*, *104*, 9809–9830.

Lugaz, N., A. Vourlidas, and I. I. Roussev (2009), Deriving the radial distances of wide coronal mass ejections from elongation measurements in the heliosphere 2013 application to CME-CME interaction, *Ann. Geophys.*, *27*, 3479–3488.

Möstl, C., M. Temmer, T. Rollett, C. J. Farrugia, Y. Liu, A. M. Veronig, M. Leitner, A. B. Galvin, and H. K. Biernat (2010), STEREO and Wind observations of a fast ICME flank triggering a prolonged geomagnetic storm on 5–7 April 2010, *Geophys. Res. Lett.*, *37*, L24103, doi:10.1029/2010GL045175.

Odstrcil, D., and V. Pizzo (1999), Three-dimensional propagation of CMEs in a structured solar wind flow: 1. CME launched within the streamer belt, *J. Geophys. Res.*, *104*, 483–492.

Odstrčil, D., M. Dryer, and Z. Smith (1996), Propagation of an interplanetary shock along the heliospheric plasma sheet, *J. Geophys. Res.*, *101*, 19,973–19,986, doi:10.1029/96JA00479.

Odstrcil, D., V. Pizzo, and C. N. Arge (2005), Propagation of the 12 May 1997 interplanetary coronal mass ejection in evolving solar wind structures, *J. Geophys. Res.*, *110*, A02106, doi:10.1029/2004JA010745.

Priest, E. R. (1982), *Solar Magneto-hydrodynamics*, D. Reidel, Dordrecht, Netherlands.

Reiner, M. J., M. L. Kaiser, J. Fainberg, and R. G. Stone (1998), A new method for studying remote Type II radio emissions from coronal mass ejection-driven shocks, *J. Geophys. Res.*, *103*, 29,651–29,664.

Riley, P., J. A. Linker, and Z. Mikic (2001), An empirically-driven global MHD model of the solar corona and inner heliosphere, *J. Geophys. Res.*, *106*, 15,889–15,901.

Rouillard, A. P., et al. (2010), Intermittent release of transients in the slow solar wind: 1. Remote sensing observations, *J. Geophys. Res.*, *115*, A04103, doi:10.1029/2009JA014471.

Rouillard, A. P., et al. (2011), Interpreting the properties of solar energetic particle events by using combined imaging and modeling of interplanetary shock, *Astrophys. J.*, *735*, 7, doi:10.1088/0004–637X/735/1/7.

Sheeley, N. R., J. H. Walters, Y.-M. Wang, and R. A. Howard (1999), Continuous tracking of coronal outflows: Two kinds of coronal mass ejections, *J. Geophys. Res.*, *104*, 24,739–24,768, doi:10.1029/1999JA900308.

Sheeley, N. R., Jr., et al. (2008), Heliospheric images of the solar wind at Earth, *Astrophys. J.*, *675*, 853–862, doi:10.1086/526422.

Steinolfson, R. S., M. Dryer, and Y. Nakagawa (1975), Numerical MHD simulation of interplanetary shock pairs, *J. Geophys. Res.*, *80*, 1223–1231, doi:10.1029/JA080i010p01223.

Thernisien, A. F. R., R. A. Howard, and A. Vourlidas (2006), Modeling of flux rope coronal mass ejections, *Astrophys. J.*, *652*, 763–773.

Toth, G., and D. Odstrcil (1996), Comparison of some flux corrected transport and total variation diminishing numerical schemes for hydrodynamic and magnetohydrodynamic problems, *J. Comput. Phys.*, *128*, 82–100.

Wood, B. E., R. A. Howard, and D. G. Socker (2010), Reconstructing the morphology of an evolving coronal mass ejection, *Astrophys. J.*, *715*, 1524–1532.

Wood, B. E., C.-C. Wu, R. A. Howard, D. G. Socker, and A. P. Rouillard (2011), Empirical reconstruction and numerical modeling of the first geoeffective coronal mass ejection of solar cycle 24, *Astrophys. J.*, *729*, 70.

Xie, H., L. Ofman, and G. Lawrence (2004), Cone model for halo CMEs: Application to space weather forecasting, *J. Geophys. Res.*, *109*, A03109, doi:10.1029/2003JA010226.

Xie, H., O. C. St. Cyr, N. Gopalswamy, S. Yashiro, J. Krall, M. Kramar, and J. Davila (2009), On the origin, 3D structure and dynamic evolution of CMEs near solar minimum, *Solar Phys.*, *259*, 143–161.

H. Cremades, UTN-FRM/CONICET, CP M5502AJE Mendoza, Argentina.

N. Gopalswamy and O. C. St. Cyr, NASA Goddard Space Flight Center, Code 670, Greenbelt, MD 20771, USA.

L. Mays, NASA Postdoctoral Program Fellow, Oak Ridge Associated Universities, Oak Ridge, TN 37831, USA.

D. Odstrcil, Department of Computational and Data Sciences, George Mason University, 4400 University Dr., MS 6A2, Fairfax, VA 22030, USA.

H. Xie, Department of Physics, Catholic University of America, 200 Hannan Hall, Washington, DC 20064, USA. (hong.xie@nasa.gov)